

# New Approach for Error Reduction in the Volume Penalization Method

Wakana Iwakami-Nakano

*Faculty of Science and Engineering, Waseda University, 3-4-1 Okubo, Shinjuku, Tokyo,  
169-8555, JAPAN*

Yuzuru Yatagai

*Department of Applied Information Sciences, Graduate School of Information Sciences,  
Tohoku University, 6-3-09 Aoba, Aramaki-aza, Aoba-ku, Sendai, Miyagi, 980-8579,  
JAPAN*

Nozomu Hatakeyama

*NICHE, Tohoku University, 6-6-10 Aoba, Aramaki-aza, Aoba-ku, Sendai, Miyagi,  
980-8579, JAPAN*

Yuji Hattori

*Institute of Fluid Science, Tohoku University, 2-1-1 Katahira, Aoba-ku, Sendai, Miyagi,  
980-8577, JAPAN*

---

## Abstract

The volume penalization method offers an efficient way to numerically simulate flows around complex-shaped bodies which move and/or deform in general. In this method a penalization term which has permeability  $\eta$  and a mask function is added to a governing equation as a forcing term in order to impose different dynamics in solid and fluid regions. In this paper we investigate the accuracy of the volume penalization method in detail. We choose the one-dimensional Burgers' equation as a governing equation since it enables us extensive study and it has a nonlinear term similar to the Navier-Stokes equations. It is confirmed that the error which consists of the discretization/truncation error, the penalization error, the round-off error, and others has the same features as those in previous results when we use the standard definition of the mask function. As the number of grid points increases, the error converges to a non-zero constant which is equal to the

penalization error. We propose a new approach for reducing the penalization error, based on the analytical solution of the one-dimensional diffusion equation with a penalization term. We modify the mask function by shifting the boundary between the solid and fluid regions by  $\sqrt{\nu\eta}$  toward the fluid region. The numerical results for the one-dimensional Burgers' equation and the two-dimensional Navier-Stokes equations show that our new approach is effective in reducing the error; the error decreases to zero as the number of grid points increases. We also found that the error reduction is enhanced for large permeability.

*Keywords:* volume penalization method, immersed boundary method, compact scheme, error reduction

---

## 1. Introduction

Flows around solid bodies have been studied in a wide variety of fields in science and engineering. In experiments it is difficult to visualize flow field and to obtain the field data in a three-dimensional space. In this regard computational fluid dynamics has advantages since the precise data are at hand. There are several kinds of space discretization methods, for example, the finite difference method, the finite volume method, the spectral method, and so on. In the finite difference and the finite volume methods, a grid system is normally generated so that the boundaries between fluid and solid regions coincide with grid lines forming a body-fitted grid system because it is easy to impose boundary conditions. On the other hand, in the spectral method a set of orthogonal functions such as Fourier series and Chebyshev polynomials are used to expand the flow variables. It is used for flows in simple geometries like periodic boundary. However, if there exist complex-shaped solid bodies or bodies which move or deform in the flow, it is difficult to generate a body-fitted grid system of high quality and to simulate the flow using the spectral method since it is hopeless to find a set of orthogonal functions with computational efficiency. The volume penalization (VP) method is one of the simplest methods that enable us to calculate flows which include solid bodies with mobility, deformability, and complex geometry.

The VP method is one of the immersed boundary (IB) methods [11]. In the IB methods an external force term is added to the equations of motion to impose boundary conditions. IB methods are classified into two types: *the continuous forcing approach* in which an external force term is added

to a continuous equation and *the discrete forcing approach* in which it is added to a discretized equation. The VP method is the former type. We can use it with the Fourier pseudo-spectral method; many flows in which multiple solid bodies exist [7, 8, 12, 13], the flows inside rigid boundaries [14, 15], and the flows around moving bodies [9] have been simulated by the VP method. Moreover, the VP method can be used with Chebyshev pseudo-spectral method, wavelet solvers, and other high-precision methods[6].

In the VP method, a solid body is regarded as porous medium. There are two types of penalization modeling. One is the  $L^2$  penalization: the N-S equation is converted to the Darcy equation in the solid body; and the other is the  $H^2$  penalization: the N-S equation is transformed to the Brinkman equation in the solid body [1, 2]. Most of the studies by VP methods have adopted the  $L^2$  penalization. The added term, called a penalization term, acts as a damping force term which has a mask function  $\chi$  and the permeability  $\eta$ . Usually the step function, which is 0 in the fluid region and 1 in the solid region, is chosen as  $\chi$ . The mask function activates the penalization term in the solid region, and the penalized N-S equation turns into the Darcy equation.

One of the advantages of the VP method is that there are rigorous results about convergence: the penalized solution converges to the solution of the original problem with no-slip boundary conditions as permeability tends to zero. Angot *et al.*[1] proved mathematically that the upper bound for the penalization error, which is the difference between the solutions of the original and penalized N-S equations, is  $O(\eta^{1/4})$  in the fluid region. Carbou and Fabrie[3] showed that this upper bound is improved to  $O(\eta^{1/2})$ . Moreover, Kevlahan and Ghidaglia[7] considered a Stokes flow over a flat plate whose dynamics is reduced to the one-dimensional diffusion equation and showed analytically that the error between the exact and penalized solutions is  $O(\eta^{1/2})$  in the fluid region. These results imply that we can make the penalization error smaller than the discretization error by choosing sufficiently small  $\eta$ .

However, we cannot choose too small value for  $\eta$  when we use an explicit method for time development. The relation  $\Delta t \leq C\eta$  should be fulfilled in order to ensure numerical stability, where  $\Delta t$  is the time step and  $C$  is a constant which depends on the method of time integration. When the total error, which is the difference between a penalized numerical solution and the exact solution to the original problem, is dominated by the penalization error, we cannot make the total error smaller than the penalization error in

the limit of large  $N$  which is the number of grid points. Keetels *et al.*[6] found that there is an optimal choice of  $N$  and  $\eta$  giving the minimum total error when the penalization error approximately compensates the truncation error. They obtained the relation between the two parameters  $N$  and  $\eta$  which give the optimal choice. If we know the two parameters in advance, we can make both the total error and the computational cost small by specifying the optimal choice of  $N$  and  $\eta$ . However, their results show that the choice depends on the space discretization method. In addition, there is usually another requirement for the size of grid spacings that comes from the smallest scale of fluid motion. Therefore, other strategies are needed to reduce the total error when we cannot choose small value for  $\eta$ .

In this paper we investigate the accuracy of the volume penalization method. The characteristics of the error of the VP method are investigated in detail for the one-dimensional (1D) Burgers' equation using various space discretization schemes. Since exact solutions are known for the 1D Burgers' equation in spite of its nonlinearity, we can evaluate the error between numerical and exact solutions explicitly. Next we propose a new approach for reducing the total error by modifying the mask function. Then we show that it is also effective for the two-dimensional (2D) N-S equations.

This paper is organized as follows. First, in Section 2 we show the results of basic studies on the VP method and propose a new method for error reduction. Next, we apply it to a 2D problem in Section 3. Finally, we conclude in Section 4.

## 2. Basic study on 1D problems

### 2.1. Statement of the problem

In this section, we are mostly concerned with the *1D Burgers' equation*

$$\frac{\partial u}{\partial t} + u \frac{\partial u}{\partial x} = \nu \frac{\partial^2 u}{\partial x^2}, \quad (1)$$

with the initial and boundary conditions

$$u(0, x) = u_0(x) = -\sin\left(\frac{\pi x}{L}\right), \quad (2)$$

$$u(t, \pm L) = 0, \quad (3)$$

where  $\nu$  denotes the diffusion coefficient. The function  $u(t, x)$  may be regarded as flow velocity as Eq. (1) is the 1D compressible N-S equation without

pressure. Kevlahan and Ghidaglia[7] considered the *1D diffusion equation* in order to investigate basic properties of the VP method. The 1D diffusion equation is desirable for validating numerical methods since it is linear so that both the original equation and the penalized equation have analytical solutions. However, the effects of nonlinearity cannot be tested. Thus we choose the simplest nonlinear equation which is related with the N-S equations and has analytical solutions for the original equation.

Exact solutions of Eqs. (1)–(3) are obtained using the formula by Cole [4]

$$u_{\text{exact}}(t, x) = 2\nu \frac{\sum_{n=1}^{\infty} (n\pi/L) \exp[-\nu n^2 \pi^2 t/L^2] A_n \sin(n\pi x/L)}{A_0 + \sum_{n=1}^{\infty} \exp[-\nu n^2 \pi^2 t/L^2] A_n \cos(n\pi x/L)}, \quad (4)$$

$$A_0 = \frac{1}{2L} \int_{-L}^L \theta_0(x) dx, \quad (5)$$

$$A_n = \frac{1}{L} \int_{-L}^L \theta_0(x) \cos \frac{n\pi x}{L} dx, \quad (6)$$

$$\theta_0(x) = C \exp \left( -\frac{1}{2\nu} \int_0^x u_0(\xi) d\xi \right). \quad (7)$$

Using the VP method, we try to obtain a numerical solution as close as possible to the analytical solution (4). We set  $L = \pi$  in the rest of the paper.

## 2.2. Numerical setups

In the VP method, the 1D Burgers' equation in Eq. (1) with the boundary conditions (3) is approximated by the equation with a penalization term

$$\frac{\partial u}{\partial t} + u \frac{\partial u}{\partial x} = \nu \frac{\partial^2 u}{\partial x^2} - \frac{\chi}{\eta} (u - u_s), \quad (8)$$

where  $u_s$  is prescribed velocity of a solid region and  $\eta$  is permeability. In this paper,  $u_s$  is basically zero,  $\nu$  is fixed to be  $10^{-1}$ , and  $\eta$  is varied from  $10^{-2}$  to  $10^{-5}$ . The mask function  $\chi$  is set to a step function,

$$\chi(x) = \begin{cases} 0 & \text{in } \Omega_f \\ 1 & \text{in } \Omega_s \end{cases}. \quad (9)$$

The whole computational domain  $\Omega = \Omega_f + \Omega_s$  covers the range  $|x| < L_b$ . The fluid region  $\Omega_f$  is defined as  $|x| \leq L$ , and  $\Omega_s$  corresponds to the solid

regions  $L \leq |x| \leq L_b$ , where  $L_b = 2\pi$ . Thus the boundaries between  $\Omega_f$  and  $\Omega_s$  are located at  $x = \pm L = \pm\pi$ . The initial condition is

$$u(0, x) = \begin{cases} -\sin(x) & \text{in } \Omega_f \\ 0 & \text{in } \Omega_s \end{cases}. \quad (10)$$

The terms containing spatial derivatives in Eq. (8) are discretized with one of the following methods: the second-order central difference method, the fourth-order central difference method, the fourth-order Padé type compact finite difference scheme [10], and the Fourier spectral method. We use a uniform mesh. The fourth-order Runge-Kutta method is used for the time marching. The time step is fixed to be  $\Delta t = 10^{-5}$ . The grid/mode number of  $N = 250 - 2750$  and the permeability of  $\eta = 10^{-5} - 10^{-2}$  are chosen to meet the conditions due to the nonlinear term  $u_{\max}\Delta t/\Delta x < C_c$ , the diffusion term  $\nu\Delta t/(\Delta x)^2 < C_d$ , and the penalization term  $\Delta t < C\eta$ , where  $u_{\max}$  is the maximum velocity and  $C_c$ ,  $C_d$ , and  $C$  are constants.

Here we consider the definition of the step function on discrete grid points. We cannot express the step function rigorously on discrete grid points since there is a non-zero gap between the grid points at which the value jumps from 0 to 1. Thus we should choose a mask function which gives the penalized numerical solution correctly converging to the penalized exact solution as  $N$  tends to  $\infty$ . Fig. 1 depicts three candidates for mask functions near the boundary between  $\Omega_s$  and  $\Omega_f$ : the boundary coincides with the grid point where  $\chi$  is 1 on Type A (Fig. 1a); the boundary is located at the midpoint between the two grid points at which the value of the mask function jumps from 0 to 1 on Type B (Fig. 1 b); the boundary coincides with the grid point where  $\chi$  is 0 on Type C (Fig. 1c). In Section 2.3 we first compare the results on Type A with previous results since it is a natural choice. Then, we determine which type of the definition of the mask functions is most suitable, and show how the errors are reduced when we modify the mask functions defined by the most suitable definition in Section 2.4.

### 2.3. Error analysis

In this section, we investigate the characteristics of the total error for Type A mask function. After showing the general features of the total error of the penalization method, we compare them with previous results.

#### 2.3.1. General features

Fig. 2 compares the numerical and exact solutions of the 1D Burgers' equation in the whole computational region (Fig. 2a) and near the boundary

between  $\Omega_s$  and  $\Omega_f$  (Fig. 2b). The numerical solutions are computed with the highest resolution until  $t = 100$ . The solutions are close to a sine wave in the fluid region and is approximately zero in the solid regions (Fig. 2a). For large values of  $\eta$ , however, the numerical solutions deviate from the exact solution (Fig. 2a) and there is leak from solid to fluid regions if we regard  $u$  as flow velocity (Fig. 2b). This deviation from the exact solution is due to the penalization term. They decrease as  $\eta$  tends to zero.

Next, we discuss the grid/mode number dependence of total errors using (a) the second-order central difference method, (b) the fourth-order central difference method, (c) the fourth-order compact difference method, and (d) the spectral method. In this study, total error  $\delta_{\text{tot}}$  is defined as the root mean square of the difference between a numerical solution and the exact solution

$$\delta_{\text{tot}} \equiv \sqrt{\frac{\int_{\Omega_f} |u(t, x) - u_{\text{exact}}(t, x)|^2 dx}{\int_{\Omega_f} dx}}, \quad (11)$$

where  $u_{\text{exact}}$  is an exact solution of the 1D Burgers' equation *without* the penalization term, obtained from Eqs.(4) – (7). The total error  $\delta_{\text{tot}}$  may be expressed as

$$\delta_{\text{tot}} = \delta_\eta + \delta_N + \delta_{\text{etc}}, \quad (12)$$

where  $\delta_\eta$ ,  $\delta_N$ , and  $\delta_{\text{etc}}$  are the penalization error, the space discretization/truncation error, and the sum of the other errors. Note that  $\delta_\eta$  and  $\delta_N$  are independent of  $N$  and  $\eta$ , respectively, and  $\delta_{\text{etc}}$  is normally negligible. The data plotted by asterisks in Fig. 3 are obtained by solving the non-penalized 1D Burgers' equation with the no-slip boundary conditions. As shown in Fig. 3 (d) for the spectral method  $\delta_{\text{tot}}$  takes a constant value of  $O(10^{-14})$ , which is regarded as the value of  $\delta_{\text{etc}}$ .

In Figs. 3 (b), (c), and (d), the optimum grid/mode number  $N_{\text{opt}}$  at which  $\delta_{\text{tot}}$  takes the minimum value is clearly observed for each value of  $\eta$ . At  $N = N_{\text{opt}}$ ,  $\delta_N$  and  $\delta_\eta$  would have the same magnitudes and opposite signs to be canceled out. For  $N > N_{\text{opt}}$  the total error  $\delta_{\text{tot}}$  tends to a constant with increasing  $N$ . In other words  $\delta_{\text{tot}}$  does not depend on  $N$  when  $N \gg N_{\text{opt}}$ , implying that  $\delta_{\text{tot}}$  is dominated by  $\delta_\eta$ . For  $N \ll N_{\text{opt}}$  the total error for all values of  $\eta$  converges to one line, implying that  $\delta_{\text{tot}}$  does not depend on  $\eta$  for  $N \ll N_{\text{opt}}$ , as  $\delta_{\text{tot}}$  is dominated by  $\delta_N$ . The dependence of  $\delta_{\text{tot}}$  on  $N$  shown above agrees with the previous results by Keetels *et al.* [6]. In the following three sections, we investigate the features of these errors in more detail.

### 2.3.2. Optimum grid/mode number at $N = N_{\text{opt}}$

Keetels *et al.* [6] performed an error analysis of the VP method for the 2D N-S equations by numerical simulation of the dipole-wall collision using the pseudo-spectral method. They found relations  $\delta_N = \alpha N^a$  and  $\delta_\eta = \beta \eta^b$ , where  $\alpha$ ,  $\beta$ ,  $a(< 0)$ , and  $b(> 0)$  are constants which depend on numerical schemes. Previous works show  $b = 0.5$ [3, 8]. In addition, the following relation is obtained

$$\eta = \left(\frac{\alpha}{\beta}\right)^{1/b} N^{a/b} \approx \gamma N^c, \quad (13)$$

where  $\gamma$  and  $c$  are also parameters, by setting  $\delta_N = -\delta_\eta$  which makes  $\delta_{\text{tot}}$  small. For a given value of  $\eta$ , the value of  $N$  determined by Eq. (13) corresponds to  $N_{\text{opt}}$ . In Figs. 3 (b), (c), and (d),  $N_{\text{opt}}$  increases with decreasing  $\eta$ , which is consistent with Eq. (13) since  $c = a/b < 0$ . Keetels *et al.* [6] suggested that we can perform the most accurate and efficient simulation if we can determine the combination of  $N$  and  $\eta$  by Eq. (13). To do this, we must specify the unknown constants  $\gamma$  and  $c$ .

Here, we obtain  $\gamma$  and  $c$  for each discretization method by substituting  $N_{\text{opt}}$  into  $N$  in Eq. (13). The relation between  $\eta$  and  $N_{\text{opt}}$  is shown in Fig. 4. The higher-order schemes have the same power  $c = -2.0$ , but they have small differences in  $\gamma$ . As seen in Fig. 3, the ranges of  $N$  giving small error are too narrow to allow the small differences between the values of  $\gamma$  for high-order schemes. For instance, if we obtain  $N_{\text{opt}}$  from the results of the spectral method and use it for simulations with a different discretization scheme, the resulting error  $\delta_{\text{tot}}$  is not small. Moreover,  $\gamma$  and  $\eta$  for the second-order central scheme are rather different from those for the higher-order schemes. We infer from Fig. 3 (a) that the second-order central scheme cannot accomplish  $\delta_N = -\delta_\eta$ .

Next, we investigate the dependence of  $\gamma$  and  $c$  on the problem. The values of  $\gamma$  and  $c$  in the present and previous studies are summarized in the Table 1. The left column shows the present study. The middle column shows the results of the parallel plate channel flow governed by the 1D diffusion equation[7]. The right column shows the results of 2D simulations of dipole-wall collision by solving the N-S equations by the spectral method or the coherent vortex simulation (CVS)[6]. Comparing the values for the second central scheme or the spectral method, it is clear that  $\gamma$  and  $c$  depend not only on the spatial discretization but also on the problems.

The above results show that it is difficult to decrease  $\delta_{\text{tot}}$  using Eq. (13)



which includes unknown parameters  $\gamma$  and  $c$ , because they are so sensitive to both the space discretization scheme and the problem that we cannot specify them to get a benefit of the error reduction. Thus we need another strategy for decreasing  $\delta_{\text{tot}}$ , which will be proposed in Section 2.4.

### 2.3.3. Penalization error for $N_{\text{opt}} \ll N$

The penalization error dominates the total error for  $N \gg N_{\text{opt}}$ . Fig. 5 (a) shows the total error  $\delta_{\text{tot}}$  in the fluid region  $\Omega_f$  as a function of  $\eta$  for the fourth-order compact scheme. The total errors are the same ones for  $N_{\text{max}} = 2500$  shown in Fig. 3 (c), which are chosen as a typical example. The total error  $\delta_{\text{tot}}$  tends to be proportional to  $\eta^{0.5}$  as  $\eta$  increases, where  $N$  is sufficiently larger than  $N_{\text{opt}}$ . The characteristics agrees with the analytical results for the dependence of the penalization error on  $\eta$  for the N-S equation [3] and the diffusion equation [7].

We also show  $\delta_{\text{tot}}$  as a function of  $\eta$  in the solid region  $\Omega_s$  (Fig. 5b). It is calculated by Eq. (11) replacing  $\Omega_f$  by  $\Omega_s$ . In the solid region,  $\delta_{\text{tot}}$  does not depend on  $N$  very much, although there are some differences between the results for the minimum grid number  $N_{\text{min}} = 300$  and for the maximum  $N_{\text{max}} = 2500$ . The dependence of  $\delta_{\text{tot}}$  on  $\eta$  varies from  $O(\eta^{0.82})$  to  $O(\eta^{0.98})$ . The same results are obtained numerically for a flow past a square cylinder [1].

As for the other space discretization methods, the results similar to above are obtained for the penalization error. To summarize the present results obtained for a nonlinear equation show the same features as those obtained by the theoretical studies [3] and the numerical studies for both the 1D diffusion equation [7] and the multi-dimensional N-S equations [1]. However, as far as we use an explicit method for time evolution with a time step which is not sufficiently small, the penalization error is much larger than the error of the conventional method of imposing boundary conditions on boundary-fitted grids (Fig. 3). This is another reason why we seek a strategy for reducing the penalization error.

### 2.3.4. Discretization error for $N \ll N_{\text{opt}}$

As can be seen in Figs. 3 (b), (c), and (d), the total error converges to a single asymptotic line which is independent of  $\eta$  as  $N$  decreases. This implies that the discretization error is the dominant component of the total error for  $N \ll N_{\text{opt}}$ . The asymptotic line is proportional to  $N^{-1}$  showing that the spatial accuracy of the simulation is first order. The convergence of the total error for the 1D channel flow by Kevlahan and Ghidaglia [7] also indicates

the first-order accuracy unless  $N \approx N_{\text{opt}}$ . According to them this low-order accuracy is due to the  $C^2$  discontinuity of the penalized exact solution at the boundaries.

In order to check it, we consider a steady solution of the 1D Burgers' equation

$$u(\infty, x) = -u_b \tanh\left(\frac{u_b}{2\nu}x\right), \quad (14)$$

which satisfies  $u(t, x) \rightarrow \mp u_b$ ,  $\partial u(t, x)/\partial x \rightarrow 0$ , and  $\partial^2 u(t, x)/\partial x^2 \rightarrow 0$  for  $1 \ll u_b|x|/2\nu$ . For this solution the effect of penalization can be minimized if the boundaries between fluid and solid regions are located sufficiently far from  $x = 0$ . We solve Eq. (8), where we set

$$u_s(t, x) = \begin{cases} u_b & \text{if } x < 0 \\ 0 & \text{if } x = 0 \\ -u_b & \text{if } x > 0 \end{cases}. \quad (15)$$

The mask function (9) is unchanged. The initial condition is given by the steady solution (14),

$$u(0, x) = \begin{cases} -u_b \tanh\left(\frac{u_b}{2\nu}x\right) & \text{in } \Omega_f \\ -u_b \operatorname{sgn}(x) & \text{in } \Omega_s \end{cases}, \quad (16)$$

where  $u_b = 1$ . We use the numerical solutions which have converged with sufficient accuracy for the error analysis below.

Fig. 6 shows the steady solutions of the 1D Burgers' equation numerically obtained using the fourth-order compact scheme with  $N = N_{\text{max}}$ . The penalized numerical solutions for  $\eta = 10^{-2}$  and  $10^{-3}$  agree well with both the non-penalized numerical solutions and the exact solutions (Fig. 6a). The gradients of the exact solution at the boundaries are almost zero (Fig. 6b). That is, the error due to the discontinuity at the boundaries is within  $\delta_{\text{etc}}$  in Eq. (12). Thus the numerical solutions can be regarded as sufficiently smooth in this problem.

Fig. 7 shows the total error as a function of  $N$  for the steady problem. Both the total error  $\delta_{\text{tot}}$  for the penalized numerical solution and that for the non-penalized numerical solution with boundary conditions decrease as  $N^{-4}$ . The accuracy of the spatial discretization scheme used in this simulation is achieved when the solution is smooth at the boundaries. Thus we conclude that the discontinuity of the exact penalized solution is responsible for the low-order accuracy of the discretization error of the penalization method.

The accuracy of the VP method may be improved by using a continuous mask function instead of the step function. However, it is not clear whether the solutions of the penalized equation with a continuous mask function converge to that of the non-penalized equation as  $\eta$  tends to zero. In this paper, we focus on the reduction of the penalization error while the reduction of the discretization error is not pursued.

#### 2.4. Error reduction method

In this section, we propose a new method for reducing the penalization error by changing the mask function. First, we determine the appropriate definition of the mask function for good convergence. Next, we modify the mask function so that the exact solutions of the penalized equation almost agrees with that of the non-penalized equations in the fluid region.

##### 2.4.1. Most suitable definition for mask functions

We have introduced three types of mask functions: the values at the boundaries are  $\chi(\pm L) = 1.0$  for Type A, 0.5 for Type B, and 0.0 for Type C (Fig. 1). The total error as a function of grid/mode number for the three types is shown in Fig. 8. We found that the values of  $\delta_{\text{tot}}$  are different among the three types. For Types B and C we note that there is no  $N_{\text{opt}}$  at which  $\delta_{\text{tot}}$  takes local minimum value in the region  $300 \leq N \leq 2750$ . That is, the numerical solutions for Type B and C cannot satisfy any conditions to meet  $\delta_N = -\delta_\eta$ . The above observation suggests that Keetels *et al.*[6] used the mask functions of Type A since  $N_{\text{opt}}$  existed in their results. However, there are also common features among the three types. For small  $N$ , the total error  $\delta_{\text{tot}}$  increases and collapses to a single line with decreasing  $N$  regardless of  $\eta$ . For large  $N$ , on the other hand,  $\delta_{\text{tot}}$  converges to a value which depends on  $\eta$  as  $N$  increases. The latter fact implies that the penalized numerical solution does not converge to the non-penalized exact solution  $u_{\text{exact}}$ . Instead it converges to the penalized exact solution  $u_{\eta \text{ exact}}$ . Therefore, we should consider the difference between the numerical solution and  $u_{\eta \text{ exact}}$  in order to compare the convergence properties among the mask functions for the three types.

Since it is difficult to obtain  $u_{\eta \text{ exact}}$ , we introduce

$$\delta_{N_{\text{max}}} \equiv \sqrt{\frac{\int_{\Omega_f} |u(t, x) - u_{N_{\text{max}}}(t, x)|^2 dx}{\int_{\Omega_f} dx}}, \quad (17)$$

where  $u_{N_{\max}}$  is the numerical solution for  $N = N_{\max}$ , to examine the convergence property of numerical solutions. If  $N_{\max} \gg N$ ,  $u_{N_{\max}}$  can be regarded to be close to  $u_{\eta \text{ exact}}$ . Fig. 9 shows the error  $\delta_{N_{\max}}$  defined above as a function of  $N$ . For all three types of mask functions  $\delta_{N_{\max}}$  decreases with increasing  $N$ . Therefore, regardless of the type of a mask function, the penalized numerical solution monotonically converges to some solution. For  $N \ll N_{\max}$  the error  $\delta_{N_{\max}}$  is proportional to  $N^{-1.0}$  for Type A,  $N^{-2.0} \sim N^{-1.0}$  for Type B, and  $N^{-1.3}$  for Type C. For Type B we have second-order accuracy for large  $\eta$ , which is the highest accuracy among the cases considered. Furthermore, we notice that as  $\eta$  increases  $\delta_{N_{\max}}$  decreases for Types B and C, while it increases for Type A.

To clarify the above results, we calculate the difference between the numerical solution and the penalized exact solution  $u_{\eta \text{ exact}}$  for a simpler problem. Let us consider the penalized 1D *diffusion* equation

$$\frac{\partial u}{\partial t} = \nu \frac{\partial^2 u}{\partial x^2} - \frac{\chi}{\eta} u, \quad (18)$$

instead of the penalized 1D *Burgers'* equation, whose exact solution is difficult to find analytically. The exact solution of Eq. (18) is

$$u_{\eta \text{ exact}}(t, x) = \begin{cases} C_+ e^{-\nu k_n'^2 t} e^{-\alpha x} & L < x \\ C_0 e^{-\nu k_n'^2 t} \sin(k_n' x) & |x| \leq L \\ C_- e^{-\nu k_n'^2 t} e^{\alpha x} & x < -L \end{cases}, \quad (19)$$

where  $k_n'$  is the wavenumber of a solution for the penalized 1D diffusion equation and  $C_{\pm}$  and  $\alpha$  are determined by the condition of  $C^1$  continuity

$$u_{\eta \text{ exact}}(t, \pm L - 0) = u_{\eta \text{ exact}}(t, \pm L + 0), \quad (20)$$

$$\frac{\partial u_{\eta \text{ exact}}}{\partial x}(t, \pm L - 0) = \frac{\partial u_{\eta \text{ exact}}}{\partial x}(t, \pm L + 0). \quad (21)$$

By setting  $C_0 = -1$ , the constants are found to be

$$C_{\pm} = \mp e^{\alpha L} \sin(k_n' L), \quad (22)$$

$$\frac{\alpha}{k_n'} = -\frac{\cos(k_n' L)}{\sin(k_n' L)}. \quad (23)$$

In addition, on substituting Eq. (19) into Eq. (18), we obtain

$$\alpha^2 = \frac{1}{\nu\eta} - k_n'^2. \quad (24)$$

We numerically solve the set of equations (23) and (24) to obtain  $\alpha$  and  $k_n'$ . We assume  $k_n'$  be  $O(1)$  while  $L$  is set to  $\pi$ . Substituting  $\alpha$  and  $k_n'$  into Eq. (19), the solution  $u_{\eta \text{ exact}}$  in Eq. (18) is determined.

Next we define  $\delta_{\eta \text{ exact}}$  as the difference between the numerical solution and the penalized exact solution

$$\delta_{\eta \text{ exact}} \equiv \sqrt{\frac{\int_{\Omega_f} |u(t, x) - u_{\eta \text{ exact}}(t, x)|^2 dx}{\int_{\Omega_f} dx}}. \quad (25)$$

The profiles of  $\delta_{\eta \text{ exact}}$  as a function of  $N$  are depicted in Fig. 10. When  $N$  is small,  $\delta_{\eta \text{ exact}}$  for the penalized 1D *diffusion* equation has the same convergence properties as  $\delta_{N_{\max}}$  for the penalized 1D *Burgers'* equation as shown in Fig. 9. Thus, we can estimate how  $\delta_{\eta \text{ exact}}$  for the penalized 1D *Burgers'* equation converges in the large limit of  $N$  by observing  $\delta_{\eta \text{ exact}}$  for the penalized 1D *diffusion* equation. For Type B  $\delta_{\eta \text{ exact}}$  tends to be proportional to  $N^{-2}$  for large  $N$ , although it is proportional to  $N^{-1}$  for small  $N$ . On the other hand, for Types A and C, the decay rate of  $\delta_{\eta \text{ exact}}$  decreases for large  $N$ . The scaling of  $\delta_{\eta \text{ exact}}$  for Types A and C is flatter than  $O(N^{-1})$  and  $O(N^{-1.2})$ , respectively. Therefore, the best definition of the mask function is Type B, which makes the numerical solutions converge to  $u_{\eta \text{ exact}}$  with second-order accuracy. In the following, we discuss in detail the accuracy and the dependence of  $\delta_{\eta \text{ exact}}$  on  $\eta$  using the mask functions Type B.

The exact solution of the penalized 1D diffusion equation has the  $C^1$  continuity because of Eqs. (20) and (21). However, the second derivative at the boundaries between  $\Omega_f$  and  $\Omega_s$  is discontinuous

$$\frac{\partial^2 u}{\partial x^2}(t, \pm L - 0) \neq \frac{\partial^2 u}{\partial x^2}(t, \pm L + 0). \quad (26)$$

The 1D diffusion equation (18) has a second derivative term. This is why the accuracy is second-order although fourth-order schemes are used for the spatial discretization. The solutions of the penalized 1D Burgers' equation

and the N-S equations are also inferred to be same as those of the penalized 1D diffusion equation.

Fig. 11 shows the solutions near the boundary for Type B. The solid line with plus symbols is the non-penalized exact solution  $u_{\text{exact}}$ . The solid lines with other symbols denote the penalized numerical solutions  $u$  and the other lines are the penalized exact solutions  $u_{\eta \text{ exact}}$ . Both  $u$  and  $u_{\eta \text{ exact}}$  approach  $u_{\text{exact}}$  as  $\eta$  decreases. However,  $u$  deviates from  $u_{\eta \text{ exact}}$  as  $\eta$  decreases. The penalized solution has a leaching area in a solid region. The width of the leaching area is

$$1/\alpha \approx \sqrt{\nu\eta}, \quad (27)$$

which is estimated by substituting Eq. (24) into Eq. (19) under the condition  $\sqrt{\nu\eta} \ll 1$ . Thus the leaching area becomes smaller with decreasing  $\eta$  as can be seen in Fig. 11. The leaching area for small  $\eta$  is too small to be resolved with  $N = N_{\text{max}} = 2750$  grid points. It is the reason why  $\delta_{\eta \text{ exact}}$  is large for small  $\eta$  (Fig. 10b).

#### 2.4.2. Modified mask functions

Substituting  $\alpha$  and  $k'_n$  obtained above into Eq. (19), the exact solution of the penalized diffusion equation is expressed as

$$u_{\eta \text{ exact}}(t, x) = \begin{cases} -e^{-\nu k_n'^2 t} \sin(k'_n L) e^{-\alpha(x+L)} & L < x \\ -e^{-\nu k_n'^2 t} \sin(k'_n x) & |x| \leq L \\ +e^{-\nu k_n'^2 t} \sin(k'_n L) e^{+\alpha(x+L)} & x < -L \end{cases}. \quad (28)$$

The exact solution of the non-penalized diffusion equation is

$$u_{\text{exact}}(t, x) = \begin{cases} 0 & L < x \\ -e^{-\nu k_n^2 t} \sin(k_n x) & |x| \leq L \\ 0 & x < -L \end{cases}, \quad (29)$$

where  $k_n = \frac{n\pi}{L}$  ( $n = 1, 2, \dots$ ). The wavenumber  $k'_n$  in Eq. (28) corresponds to the closest  $k_n$ . We set  $L = \pi$ . Comparing Eqs. (28) and (29), it is legitimate to *shift* the mask function replacing  $L$  by  $L_{\text{VP}}$  so that  $k'_n = k_n$ . Then the relation (23) turns out to be

$$\frac{\sin k_n L_{\text{VP}}}{\cos k_n L_{\text{VP}}} = -\frac{k_n}{\alpha}. \quad (30)$$

Substituting

$$L_{\text{VP}} = L + \epsilon, \quad (31)$$

into Eq. (30) we obtain

$$\frac{\sin(k_n L) \cos(k_n \epsilon) + \cos(k_n L) \sin(k_n \epsilon)}{\cos(k_n L) \cos(k_n \epsilon) - \sin(k_n L) \sin(k_n \epsilon)} = -\frac{k_n}{\alpha}, \quad (32)$$

Assuming  $|k_n \epsilon| \ll 1$  Eqs. (27) and (32) give

$$\epsilon \approx -\sqrt{\nu\eta}. \quad (33)$$

Therefore, by setting the boundaries at  $x = \pm L_{VP} = \pm(L - \sqrt{\nu\eta})$  we obtain the penalized numerical solutions of which wavenumber  $k'_n$  almost coincides with  $k_n$ .

The original and shifted mask functions for Type B near the solid boundary are shown in Fig. 12. The original boundaries are located at  $x = \pm L = \pm\pi$ , shown by the thin broken lines. The shifted function is

$$\chi(x) = \begin{cases} 0 & \text{in } \Omega'_f \\ 1 & \text{in } \Omega'_s \end{cases}. \quad (34)$$

where  $\Omega'_f$  is  $|x| \leq L_{VP}$  and  $\Omega'_s$  is  $L_{VP} \leq |x| \leq L_b$ . The shifted boundary  $x = -L_{VP}$  is shown by the thin solid line in Fig. 12 (b). Since the distance between the grid points is adjusted to shifted the mask function, the overall numerical domain  $\Omega'$ , which is  $|x| \leq L_b$ , depends on  $N$  although  $L_b$  is close to  $2\pi$ .

The total error  $\delta'_{\text{tot}}$  for the shifted mask function is defined by Eq. (11), replacing  $\Omega_f$  by  $\Omega'_f$ . The total error  $\delta'_{\text{tot}}$  is shown as a function of  $N'$  for the penalized 1D diffusion equation in Fig. 13, where  $N' = L/(L_b/N)$  is the grid/mode number. The error  $\delta'_{\text{tot}}$  is almost same with  $\delta_{\eta \text{ exact}}$ . By modifying the mask function the total error decreases as  $N$  increases instead of converging to a non-zero constant; that is, the penalized numerical solutions converge to the non-penalized exact solutions. Since the 1D diffusion equation is linear the Fourier modes of the solutions evolve independently of each other. Thus we can simply regard that each mode whose wavenumber is  $k_n$  is converted to the corresponding mode whose wavenumber is  $k'_n$  by shifting the boundaries between fluid and solid regions by  $\sqrt{\nu\eta}$ .

We verify whether the above shifted mask function is also effective for the nonlinear 1D Burgers' equation. Fig. 14 shows the total error  $\delta'_{\text{tot}}$  as a function of  $N'$ . The convergence of  $\delta'_{\text{tot}}$  for the 1D Burgers' equation has the same characteristics with that for the diffusion equation shown in

Fig. 13. The penalized numerical solutions obtained by using the shifted mask functions converge to the exact solutions of the 1D Burgers' equation for  $-L_{VP} < x < L_{VP}$ . The nonlinear term in the 1D Burgers' equation makes the Fourier modes interact with each other producing the high wavenumber modes from the low wavenumber modes. Nevertheless, the new technique of modifying the mask function gives the same effect on the numerical solutions of the nonlinear Burgers' equation. Compared with the case of normal mask functions in Fig. 8 (b), the total error for the shifted mask functions is reduced for large  $N$ , especially for large  $\eta$ . A possible reason for the  $\eta$  dependence is discussed in the last paragraph of the section 2.4.1.

Finally, we discuss limitation of our approach. The solutions of the 1D Burgers' equation are shown for various methods in Fig. 15. The dashed lines are the original boundaries  $\pm L$  between  $\Omega_s$  and  $\Omega_f$ , and the solid line is one of the shifted boundaries  $\pm L_{VP}$  between  $\Omega'_s$  and  $\Omega'_f$ . In Fig. 15(a), the numerical solution for the shifted mask function agrees with the exact solution of the non-penalized 1D Burgers' equation, while the numerical solution for the normal mask function deviates from the exact solution. Close look at the boundary shown in Fig. 15 (b) reveals that the numerical solution for the shifted mask function agrees well with the exact solution for  $-L_{VP} < x < L_{VP}$ . However, there is a small difference between them in the vicinity of the boundaries for  $L_{VP} < |x| < L$ . This difference cannot be eliminated by our new approach.

### 3. Application to 2D problem

In the previous section we have proposed a new method to reduce the penalization error. In this section we apply it to the penalized 2D N-S equations and see whether it is effective.

#### 3.1. Numerical setups

We perform numerical simulation by solving 2D N-S equations with a penalization term

$$\frac{\partial \mathbf{u}}{\partial t} + \mathbf{u} \cdot \nabla \mathbf{u} = -\frac{1}{\rho_0} \nabla p + \nu \nabla^2 \mathbf{u} - \frac{\chi}{\eta} (\mathbf{u} - \mathbf{u}_s), \quad (35)$$

$$\nabla \cdot \mathbf{u} = 0, \quad (36)$$

where  $\mathbf{u} = (u, v)$ , and  $\mathbf{u}_s = (u_s, v_s)$ , are the flow velocity and velocity in the solid region, respectively. In Eq. (35),  $p$  is pressure,  $\rho_0$  is density which



is constant,  $\nu$  is fixed to  $10^{-2}$ , and  $\eta$  is set to  $10^{-2}$ ,  $10^{-3}$ , and  $10^{-4}$ . The normal-type mask function is

$$\chi(\mathbf{x}) = \begin{cases} 0 & \text{in } \Omega_f \\ 1 & \text{in } \Omega_s \end{cases}, \quad (37)$$

and the shifted-type mask function is described as

$$\chi(\mathbf{x}) = \begin{cases} 0 & \text{in } \Omega'_f \\ 1 & \text{in } \Omega'_s \end{cases}. \quad (38)$$

The polar coordinate system  $(r, \theta)$  is also used in the following. We consider the Taylor-Couette flow between two co-axial cylinders. The inner and outer cylinders have the radii  $R_1$  and  $R_2$ , and they rotate with the angular velocities  $\omega_1$  and  $\omega_2$ , respectively. The overall computational domain  $\Omega$  is  $-\pi \leq x, y \leq \pi$ . The fluid region  $\Omega_f$  is defined as  $R_1 \leq r \leq R_2$ . The solid region  $\Omega_s$  consists of the inner solid region  $\Omega_{s1} = \{(x, y) \mid 0 \leq r < R_1\}$  and the outer solid region  $\Omega_{s2} = \{(x, y) \mid R_2 < r \in \Omega\}$ . For the shifted-type mask function, we define  $\Omega'_f = \{(x, y) \mid R_1 + \sqrt{\nu\eta} \leq r \leq R_2 - \sqrt{\nu\eta}\}$ ,  $\Omega'_{s1} = \{(x, y) \mid 0 \leq r < R_1 + \sqrt{\nu\eta}\}$ , and  $\Omega'_{s2} = \{(x, y) \mid R_2 - \sqrt{\nu\eta} < r \in \Omega\}$ .

The azimuthal component of velocity  $u_{\theta s}$  is set to

$$u_{\theta s}(x) = \begin{cases} 0 & \text{in } \Omega_f \\ r\omega_1 & \text{in } \Omega_{s1} \\ r\omega_2 & \text{in } \Omega_{s2} \end{cases}, \quad (39)$$

and the radial component  $u_{rs}$ , is zero all over the computational domain. The Taylor-Couette flow is given by

$$u_{\theta}(0, x) = \begin{cases} \frac{\omega_2 R_2^2 - \omega_1 R_1^2}{R_2^2 - R_1^2} r + \frac{(\omega_1 - \omega_2) R_1^2 R_2^2}{R_2^2 - R_1^2} \frac{1}{r} & \text{in } \Omega_f \\ r\omega_1 & \text{in } \Omega_{s1} \\ r\omega_2 & \text{in } \Omega_{s2} \end{cases}, \quad (40)$$

which is used as the initial condition, while the radial component  $u_r(0, x)$  is zero in the whole computational domain.[16]. In this study, we set  $\omega_1 = 1$ ,  $\omega_2 = 0$ ,  $R_1 = 0.4\pi$ , and  $R_2 = 0.8\pi$ .

The Fourier pseudo-spectral method and the fourth-order Runge-Kutta method are used for spatial and time discretization, respectively. The mode number  $N$  is varied from 256 to 4096. The time step  $\Delta t$  is  $10^{-4}$  or  $10^{-5}$  depending on  $N$  to meet the numerical stability condition.

Fig. 16 shows the mask functions near the inner cylinder at various angles. Because the boundaries between  $\Omega_s$  and  $\Omega_f$  ( $\Omega'_s$  and  $\Omega'_f$ ) are circular, the radial position of the actual boundary depends on the angle.

### 3.2. Error analysis and validation

In this section, we examine the characteristics of the total error for the 2D problem, and demonstrate the general applicability of our new approach.

The total error  $\delta_{\text{tot}}$  as a function of  $N$  for the normal and shifted mask functions are shown in Fig. 17. The total error  $\delta_{\text{tot}}$  calculated by Eq. (11) decreases as  $N$  increases showing second-order accuracy for the shifted mask functions, while it converges to a constant value for large  $N$  for the normal type mask functions. Moreover, the effect of error reduction increases with  $\eta$ . It is the same feature as that for the 1D diffusion and Burgers' equations (Figs. 13 and 14). This result shows that our new method for error reduction is also effective for the 2D N-S problem.

The solutions in the whole region, near the inner boundary, and near the outer boundary are shown in Fig. 18. The Taylor-Couette flow is well resolved by the pseudo-spectral method in all cases (Fig. 18a). Looking at the vicinity of the inner and outer cylinders, however, we observe some differences between the numerical and the exact solutions (Figs. 18b and c). The results obtained by the normal type mask function are smaller/larger near the inner/outer boundary than the exact solution. By shifting the mask function toward the fluid region by  $\sqrt{\nu\eta}$ , the numerical solution agrees well with the exact solution in the fluid region except for the immediate vicinity of the cylinders. These features are exactly the same as those of the 1D Burgers' equation. In addition, the radial distributions for  $\theta = 0^\circ$  and  $\theta = 45^\circ$  are in good agreement with each other for  $N > 1000$ . Thus, the effect of error reduction is independent of the azimuthal angle for large  $N$  although the grid system is not axisymmetric.

## 4. Summary

We have investigated the error of the volume penalization method, and have proposed a new method for reducing the error due to the penalization term. Our findings are summarized below.

First, we analyzed the error of numerical solutions of the 1D Burgers' equation with a penalization term. We used the mask function Type A, whose value at the boundaries is 1.0. The features of the total error as a function of

grid/mode number  $N$  are almost the same as those in previous works. There is an optimum grid/mode number  $N_{\text{opt}}$  depending on the permeability  $\eta$  at which the total error takes a minimum value. The total error decreases as  $N$  increases for  $N \ll N_{\text{opt}}$ , in which the discretization error is dominant. On the other hand, the total error becomes constant as  $N$  increases for  $N \gg N_{\text{opt}}$  in which the penalization error is dominant. We tried to find how to specify  $N_{\text{opt}}$  to reduce the error. However, it turned out to be difficult to specify  $N_{\text{opt}}$  in advance, because  $N_{\text{opt}}$  depends on both the space discretization method and the problem under consideration.

Next, we modified the mask function in order to reduce the total error. We found that the mask function Type B, for which the boundary is located at the midpoint of the grid points where the mask function jumps from 0 to 1, makes the numerical penalized solutions converge to the exact penalized solutions. Although Keetels *et al.*[6] seem to have used the mask function Type A, it is important to use the mask function Type B to reduce the penalization error. Our new idea is to shift the boundary between fluid and solid regions of the mask function toward the fluid region by  $\sqrt{\nu\eta}$ . The modified mask function makes the total error decrease as  $N$  increases so that the penalization error is significantly reduced. Since the leaking area in the solid region should be adequately resolved for given  $N$  to obtain the effect of error reduction, this technique is effective for comparatively large  $\eta$ . Thus it is useful when the explicit method is used for time integration because of the condition for numerical stability  $\Delta t < C\eta$ .

Finally, we performed two-dimensional numerical simulations of Taylor-Couette flow between two co-axial cylinders to confirm the applicability of the present method. The results showed that modifying the mask function is also effective for two-dimensional incompressible Navier-Stokes equation even if circular solid boundaries are immersed in the Cartesian grids. Therefore, it would be valid for various governing equations, space discretization methods, and multi-dimensional problems.

There are several conditions for permeability  $\eta$ , some of which are mentioned above: (i) time resolution: response time  $\eta$  should be smaller than the smallest time scale which should be resolved; (ii) spatial resolution: the “surface thickness”  $\sqrt{\nu\eta}$  should be smaller than the smallest length scale which should be resolved; (iii) resolution at the boundaries: the grid spacing should be smaller than  $\sqrt{\nu\eta}$  to resolve the surface “layer” at the boundaries; (iv) numerical stability for explicit time integration:  $\Delta t < C\eta$ . The conditions (i) and (ii) are necessary, while (iii) is optional and (iv) is irrelevant when an

implicit method is used for time integration.

In this study, we did not discuss the applicability of our error reduction method for the non-uniform grid, moving or deforming solid boundaries, volume penalization method for compressible flow, and so on. Furthermore, we do not deal with continuous mask functions[9]. These problems are important for development of the volume penalization method and will be investigated as future works.

## **Acknowledgments**

Numerical calculations were performed on the Altix UV1000 at the Institute of Fluid Science, Tohoku University. This study was partially supported by the academic research grant by Maekawa Houonkai in 2011.

Table 1: Summary of the values of  $\gamma$  and  $c$  for the relational expression of  $\eta = \gamma N_{\text{opt}}^c$  in the present and previous studies.

	1D Burgers sine wave	1D diffusion parallel plate channel by Kevlahan (2001)	2D N-S dipole-wall collision by Keetels (2007)
2nd central	$\gamma \sim 13000$ $c = -3.1$	$c = -3.0$	
4th central	$\gamma \sim 110$ $c = -2.0$		
4th compact	$\gamma \sim 130$ $c = -2.0$		
Spectral Fourier	$\gamma \sim 155$ $c = -2.0$	$c = -2.3$	$\gamma \sim O(10^5)$ $c = -3.6$
CVS Wavelet			$\gamma \sim O(10^2)$ $c = -1.5$

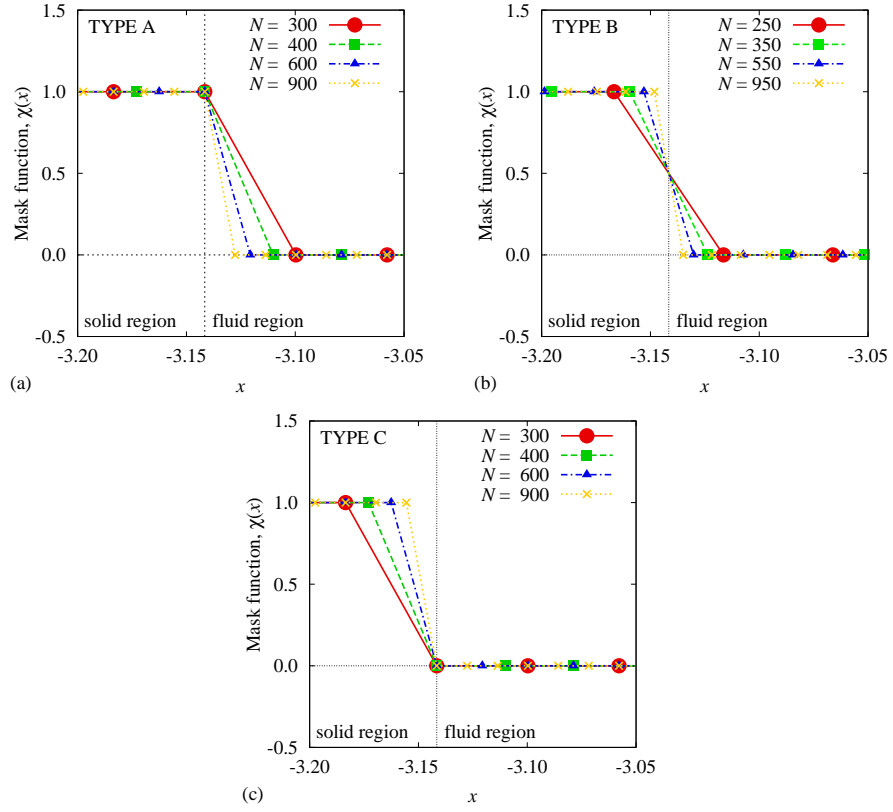


Figure 1: The mask function for (a) Type A, (b) Type B, and (c) Type C.

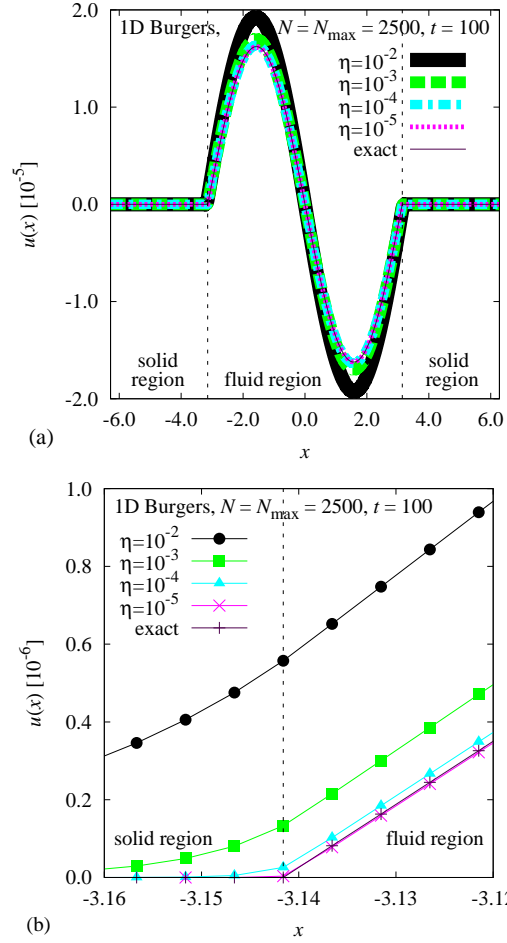


Figure 2: The distribution of solutions for the 1D Burgers' equation (a) in the whole region and (b) near the solid boundary.

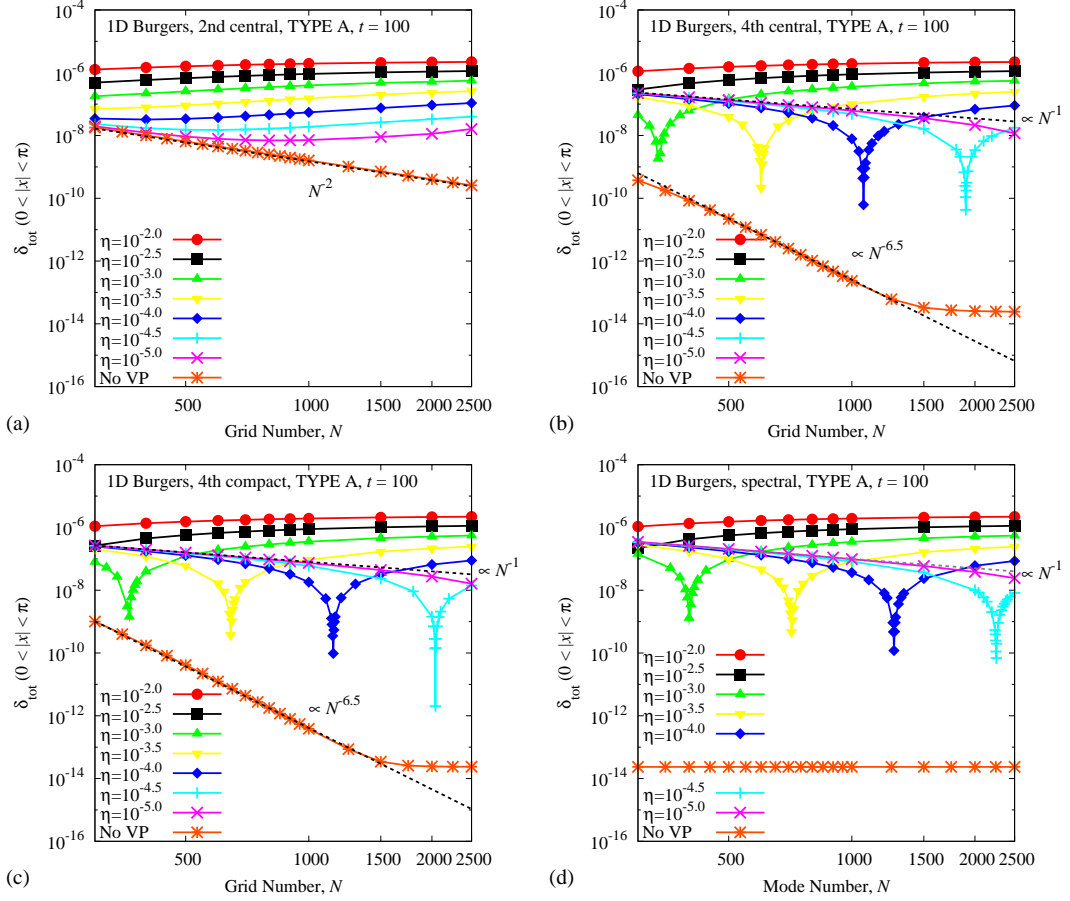


Figure 3: The total error  $\delta_{\text{tot}}$  as a function of  $N$  for the various discretization methods: (a) the second-order central difference scheme; (b) the fourth-order central difference scheme; (c) the fourth-order compact difference scheme; (d) the spectral method.



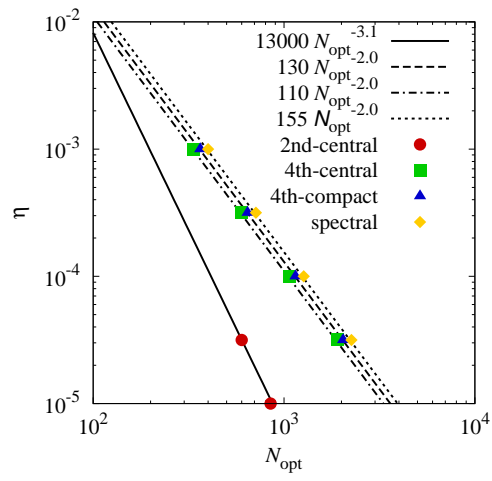


Figure 4: The relation between the permeability  $\eta$  and the optimum grid/mode number  $N_{\text{opt}}$ .

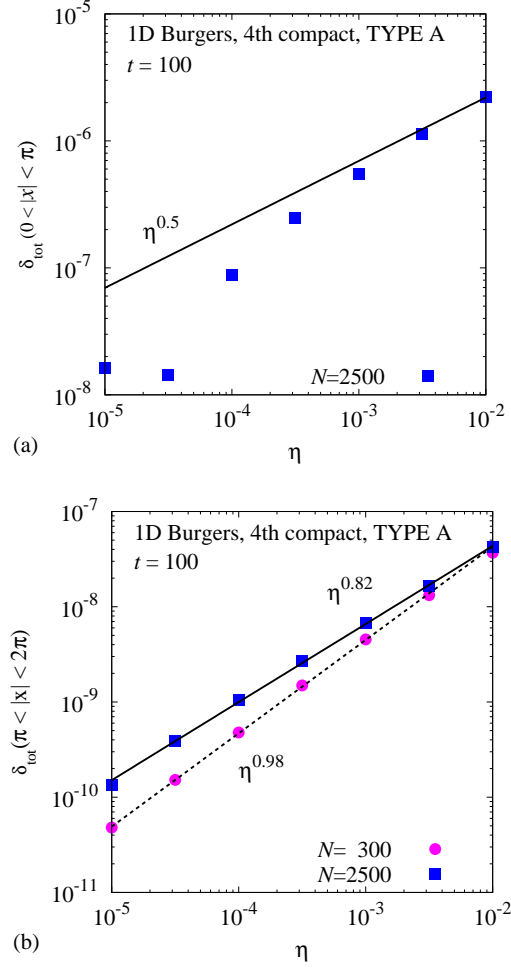


Figure 5: The total error  $\delta_{\text{tot}}$  as a function of  $\eta$  in (a) the fluid region  $\Omega_f$  and (b) the solid region  $\Omega_s$ .

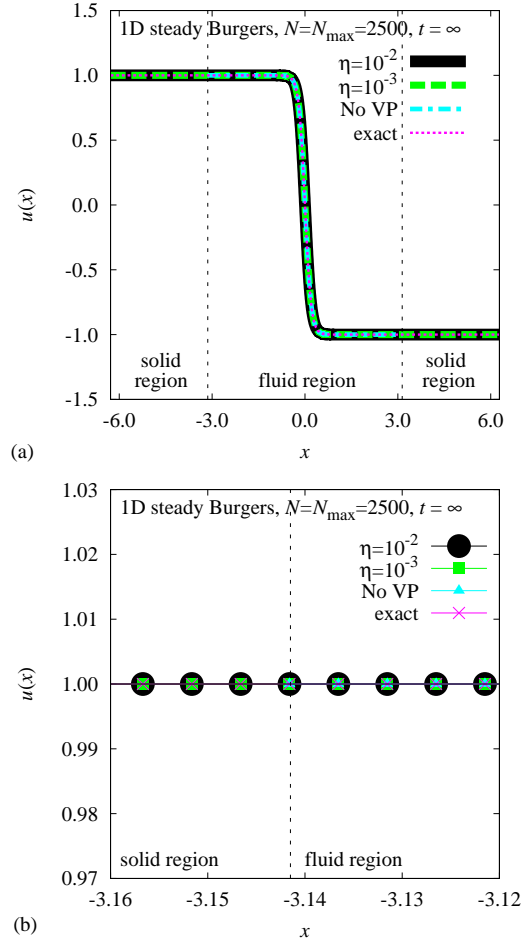


Figure 6: The steady solutions of the 1D Burgers' equation (a) in the whole region and (b) near the solid boundary. The numerical solutions are obtained using the fourth-order compact scheme.

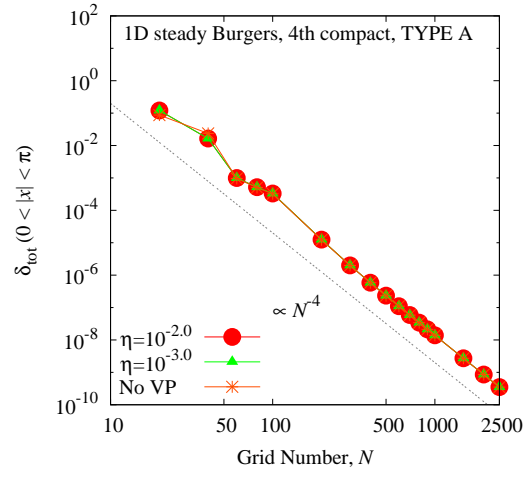


Figure 7: The total error  $\delta_{\text{tot}}$  as a function of  $N$  for the steady numerical solutions of 1D Burgers' equation solved with the fourth-order compact scheme.

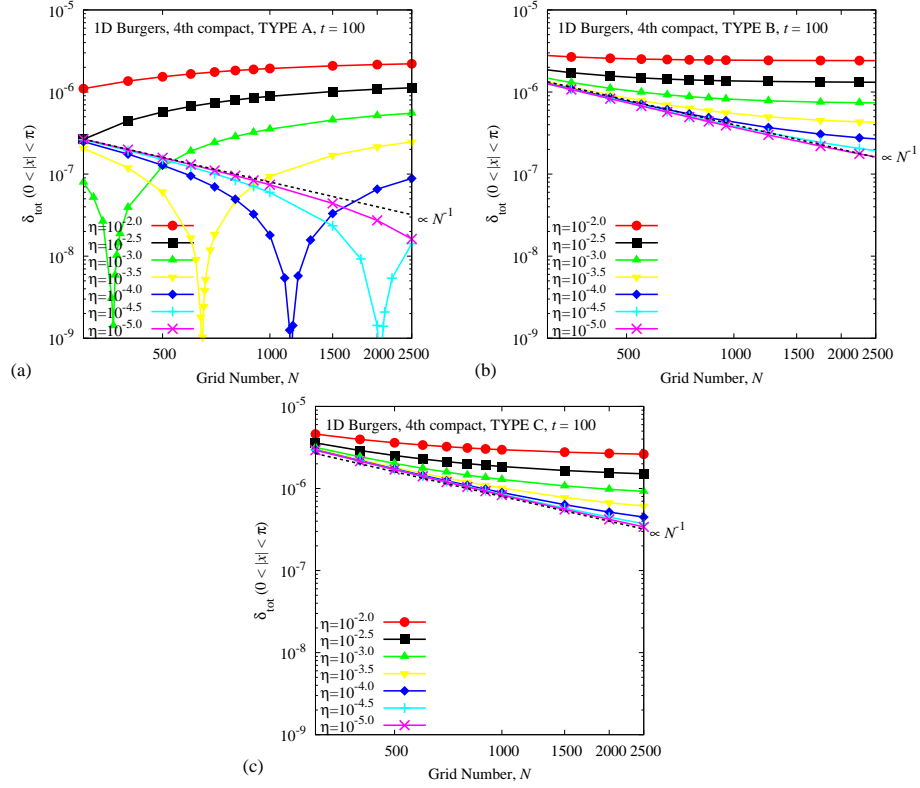


Figure 8: The total error  $\delta_{\text{tot}}$  as a function of  $N$  for the numerical solutions of the 1D Burgers' equation using the mask function for (a) Type A, (b) Type B, and (c) Type C.

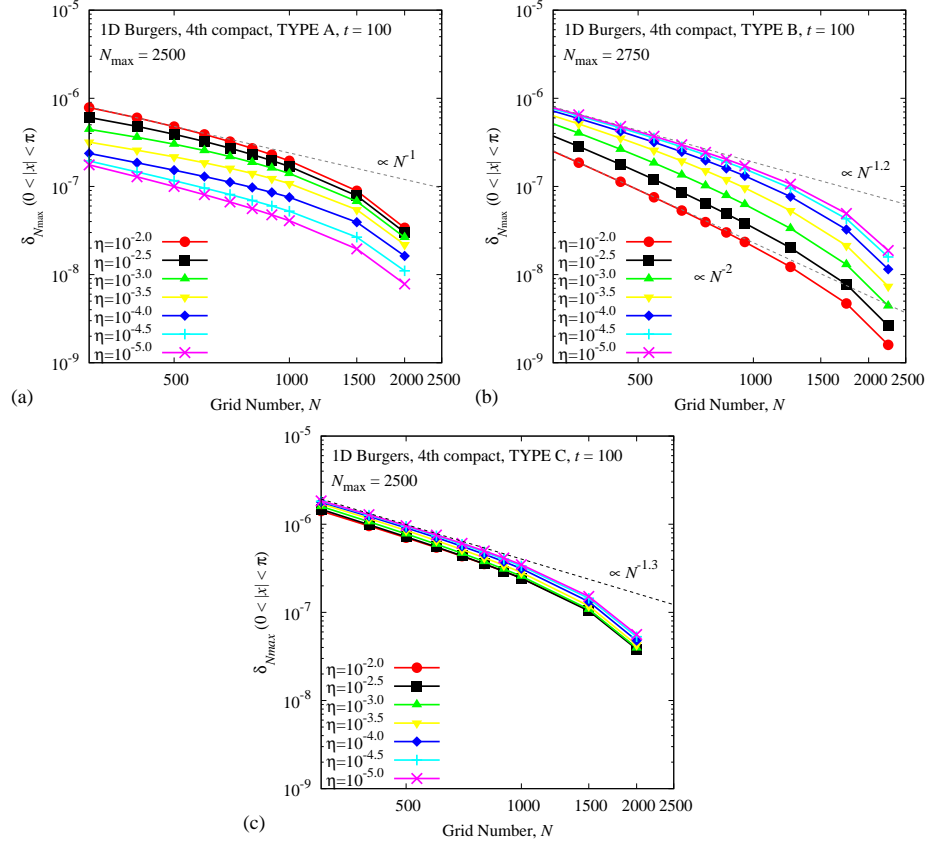


Figure 9: The error  $\delta_{N_{\max}}$  between the numerical solutions at  $N$  and  $N_{\max}$  for the 1D Burgers' equation using the mask functions for (a) Type A, (b) Type B, and (c) Type C.

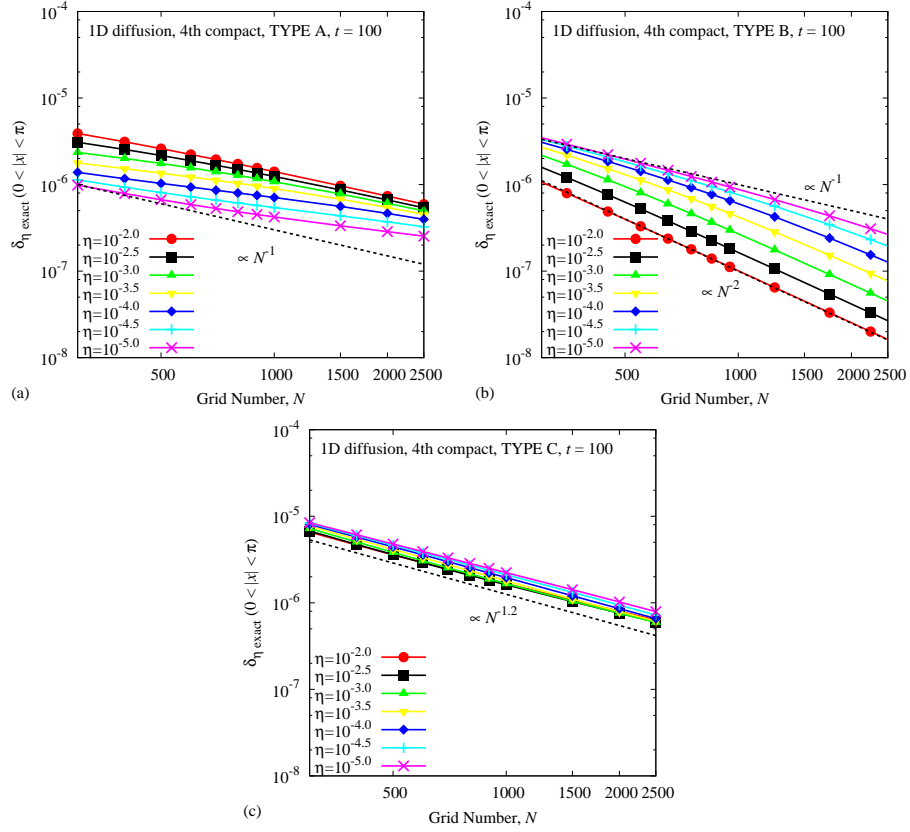


Figure 10: The error  $\delta_{\eta \text{ exact}}$  between the numerical solutions  $u$  and the exact penalized solutions  $u_{\eta \text{ exact}}$  for the 1D diffusion equation using the mask functions for (a) Type A, (b) Type B, and (c) Type C.

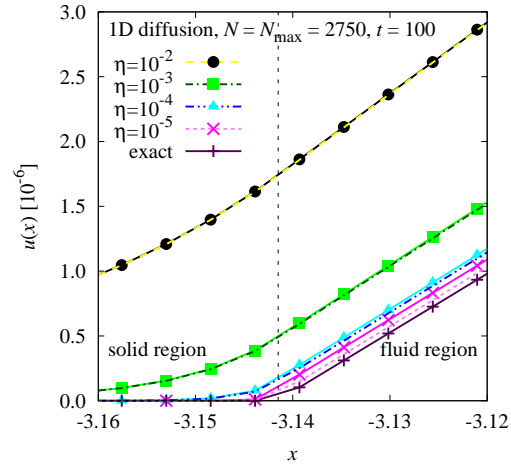


Figure 11: The numerical and exact solutions for the 1D diffusion equation using the Type B mask function.



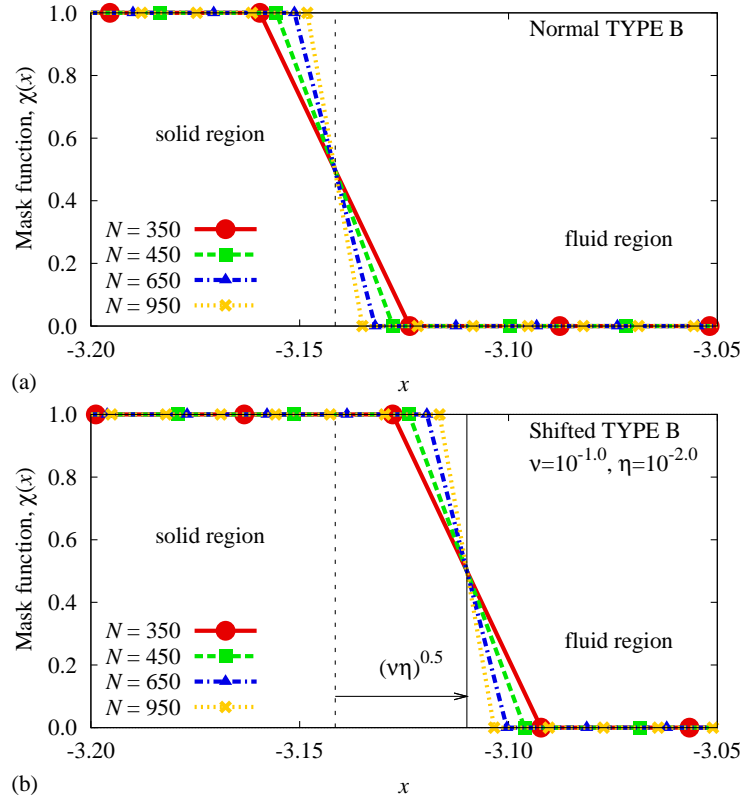


Figure 12: The normal and shifted mask functions for Type B near the solid boundary.

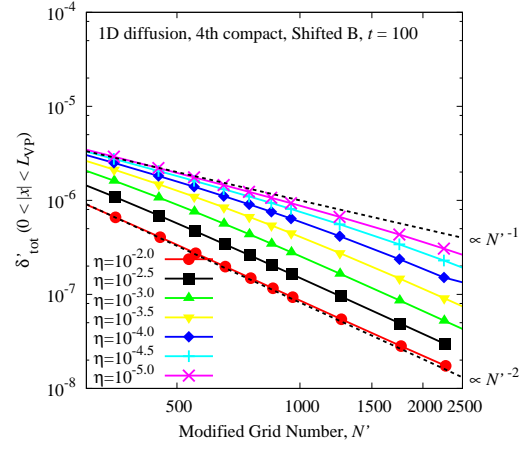


Figure 13: The total error  $\delta'_{\text{tot}}$  as a function of  $N'$  for the 1D penalized diffusion equation with shifted mask functions for Type B.

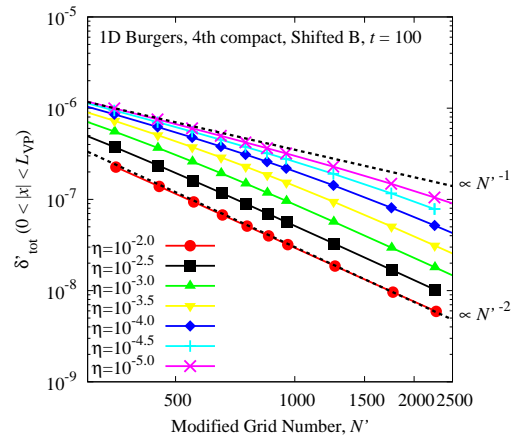


Figure 14: The total error  $\delta'_{\text{tot}}$  as a function of  $N'$  for the 1D penalized Burgers' equation with the shifted mask functions for Type B.

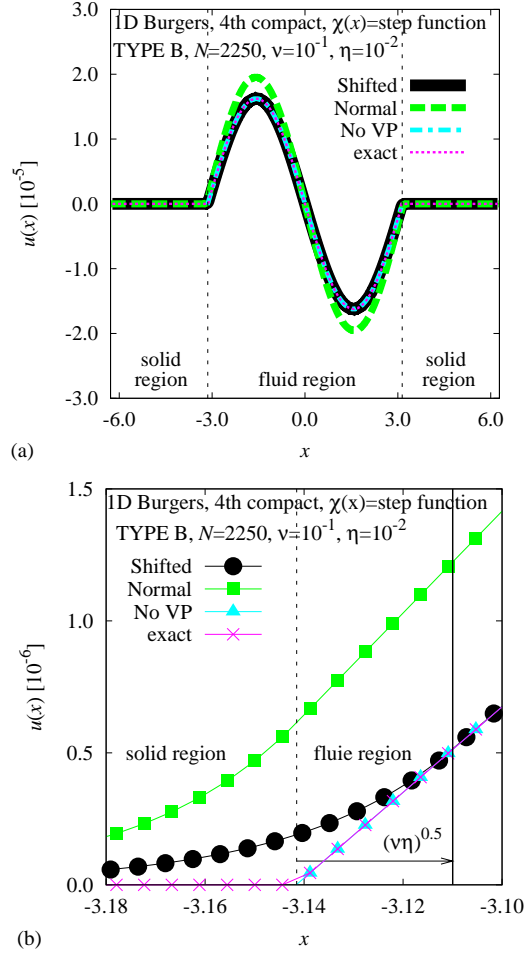


Figure 15: The comparison of the solutions for the 1D Burgers' equation (a) in the whole region and (b) near the solid boundary.

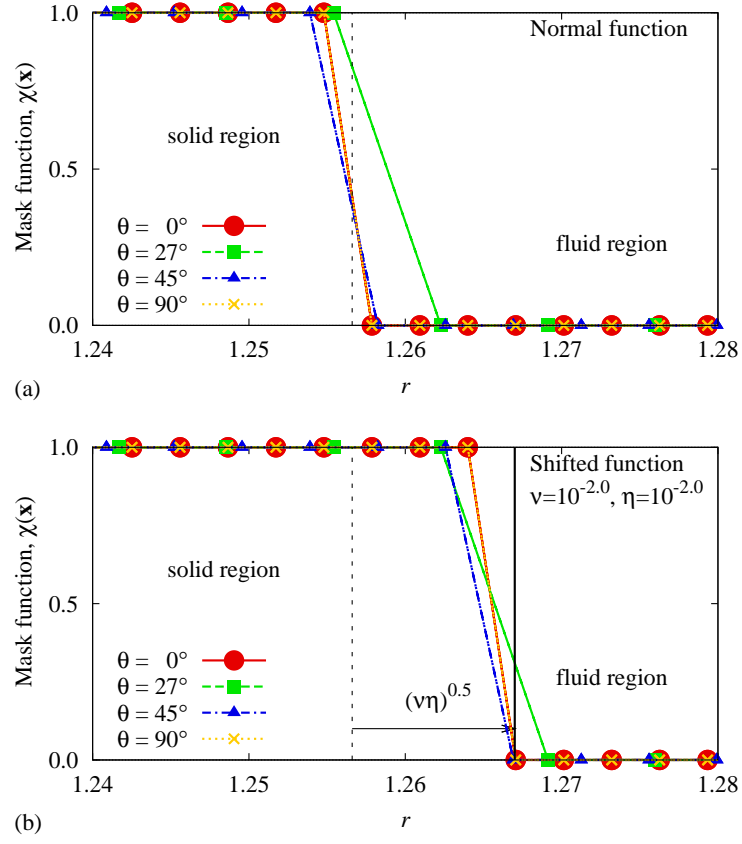


Figure 16: The distributions of  $\chi(x)$  near the inner cylinder for the 2D problem: (a) the normal mask functions, (b) the shifted mask functions.

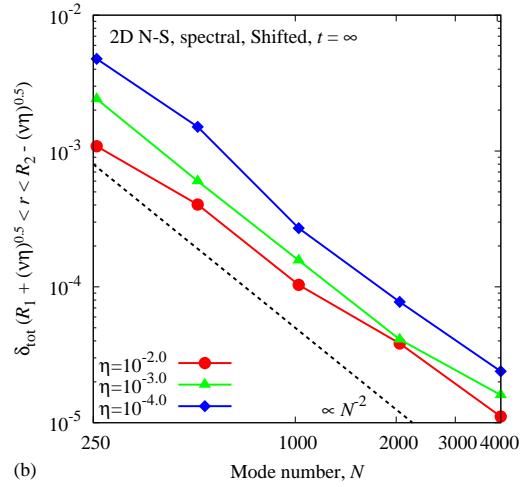
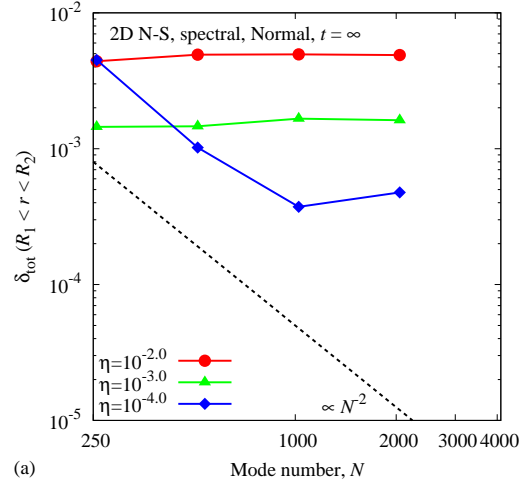


Figure 17: The characteristics of  $\delta_{\text{tot}}$  as a function of  $N$  for the 2D N-S equations: (a) the normal mask functions, (b) the shifted mask functions.

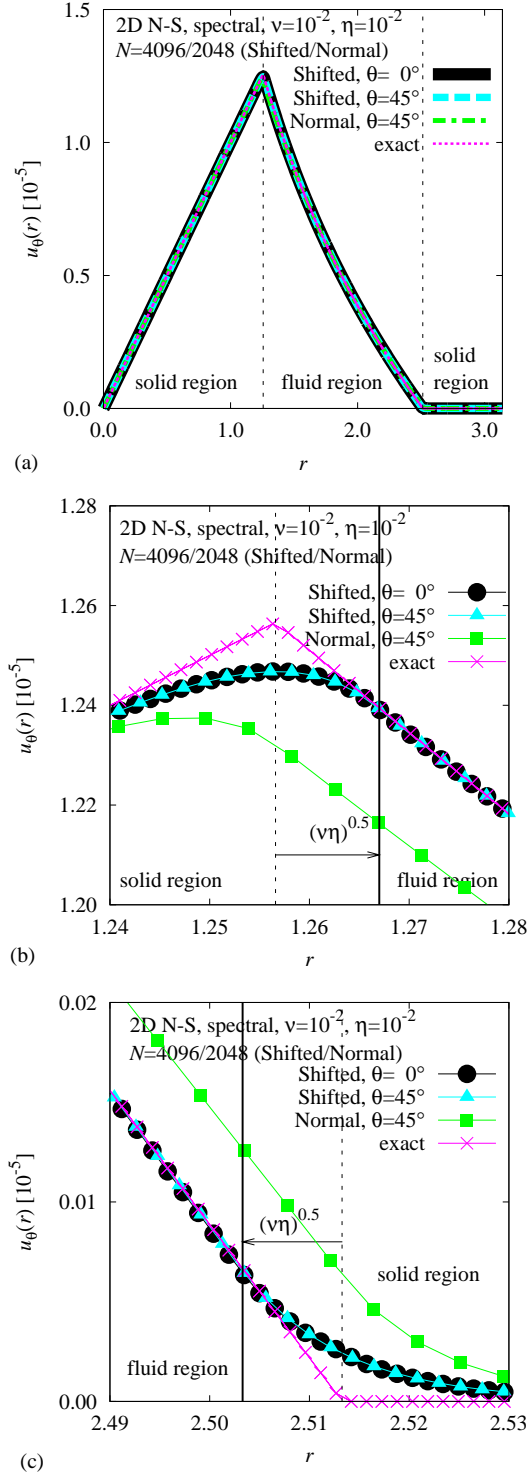


Figure 18: The comparison of solutions for 2D N-S equations. The radial distributions of azimuthal velocity are shown (a) in the whole region, (b) near the inner cylinder, and (c) near the outer cylinder.

## References

- [1] P. Angot, C.-H. Bruneau, P. Fabrie, A penalization method to take into account obstacles in incompressible viscous flows 81 (1999) 497–520.
- [2] H. C. Brinkman, Appl. Sci. Res., 1 (1949) 27–34.
- [3] G. Carbou, P. Fabrie, Adv. Differ. Equat., 8 (2003) 1453–.
- [4] J. D. Cole, Quarterly of Applied Mathematics, 9 (1951)
- [5] H. Darcy, Les fontaines publiques de la ville de Dijon, (2008) 590–594.
- [6] G.H. Keetels, U. D’Ortona, W. Kramer, H. J. H. Clercx, K. Schneider, G. J. F. van Heijst, Fourier spectral and wavelet solvers for the incompressible Navier-Stokes equations with volume-penalization: Convergence of a dipole-wall collision, J. Comput. Phys. 227 (2007) 919–945.
- [7] N. K.-R. Kevlahan, J.-M. Ghidaglia, Computation of turbulent flow past an array of cylinders using a spectral method with Brinkman penalization, Eur. J. Mech. B - Fluids 20 (2001) 333–350.
- [8] N. K.-R. Kevlahan, J. Wadsley, Suppression of three-dimensional flow instabilities in tube bundles, J. Fluid. Struct. 20 (2005) 611–620.
- [9] D. Kolomenskiy, K. Schneider, A fourier spectral method for the Navier-Stokes equations with volume penalization for moving solid obstacles, J. Comput. Phys. 228 (2009) 5687–5709.
- [10] S. K. Lele, J. Comp. Phys. 103 (1992), 16–42.
- [11] R. Mittal, G. Iaccarino, Immersed boundary methods, Annu. Rev. Fluid Mech. 37 (2005) 239–261.
- [12] K. Schneider, Numerical simulation of the transient flow behaviour in chemical reactors using a penalization method, Computers & Fluids 34 (2005) 1223–1238.
- [13] K. Schneider, M. Farge, Numerical simulation of the transient flow behaviour in tube bundles using a volume penalization method, Journal of Fluids and Structures 20 (2005) 555–566.



- [14] K. Schneider, M. Farge, Decaying two-dimensional turbulence in a circular container, *Phys. Rev. Lett.* 95 (2005) 244502.
- [15] K. Schneider, M. Farge, Final states of decaying 2D turbulence in bounded domains: influence of the geometry, *Physica D* 237 (2008) 2228–2233.
- [16] D. J. Tritton, *Physical Fluid Dynamics*, Second Edition, Oxford University Press Inc., Newyork, (1988).